

# ICES REPORT 17-15

---

June 2017

## Quantification of a Maximum Injection Volume of CO<sub>2</sub> without Geomechanical Perturbations Using a Compositional Fluid Flow Reservoir Simulator

by

Hojung Jung, Gurpreet Singh, D. Nicolas Espinoza, Mary F. Wheeler



**The Institute for Computational Engineering and Sciences**  
The University of Texas at Austin  
Austin, Texas 78712

*Reference: Hojung Jung, Gurpreet Singh, D. Nicolas Espinoza, Mary F. Wheeler, "Quantification of a Maximum Injection Volume of CO<sub>2</sub> without Geomechanical Perturbations Using a Compositional Fluid Flow Reservoir Simulator," ICES REPORT 17-15, The Institute for Computational Engineering and Sciences, The University of Texas at Austin, June 2017.*

# Quantification of a Maximum Injection Volume of CO<sub>2</sub> without Geomechanical Perturbations Using a Compositional Fluid Flow Reservoir Simulator

Hojung Jung<sup>1</sup>, Gurpreet Singh<sup>2</sup>, D. Nicolas Espinoza<sup>1\*</sup>, and Mary F. Wheeler<sup>2</sup>

<sup>1</sup> Department of Petroleum and Geosystems Engineering, The University of Texas at Austin

<sup>2</sup> Center for Subsurface Modeling, The University of Texas at Austin

\*Corresponding author: [espinoza@austin.utexas.edu](mailto:espinoza@austin.utexas.edu), 200 E Dean Keeton, Austin, 78702, USA

## Abstract

Subsurface CO<sub>2</sub> injection and storage alters formation pressure. Changes of pore pressure may result in fault reactivation and hydraulic fracturing if the pressure exceeds corresponding thresholds. Most simulation models predict such thresholds utilizing relatively homogeneous reservoir rock models and do not account for CO<sub>2</sub> dissolution in the brine phase to calculate pore pressure evolution. This article presents an estimation of reservoir capacity in terms of allowable injection volume and rate utilizing the Frio CO<sub>2</sub> injection site in the coast of the Gulf of Mexico as a case study. The work includes laboratory core testing, well-logging data analyses, and reservoir numerical simulation. We built a fine-scale reservoir model of the Frio pilot test in our in-house reservoir simulator IPARS (Integrated Parallel Accurate Reservoir Simulator). We first performed history matching of the pressure transient data of the Frio pilot test, and then used this history-matched reservoir model to investigate the effect of the CO<sub>2</sub> dissolution into brine and predict the implications of larger CO<sub>2</sub> injection volumes. Our simulation results including CO<sub>2</sub> dissolution exhibited 33% lower pressure build-up relative to the simulation excluding dissolution. Capillary heterogeneity helps spread the CO<sub>2</sub> plume and facilitate early breakthrough. Simulation results suggest that injection rates adopted during the actual pilot test very likely did not effect the mechanical integrity of the storage complex. Fault reactivation requires injection volumes of at least ~100,000 tons of CO<sub>2</sub> (~ sixty times the actual injected volume). Hydraulic fracturing necessitates much larger injection rates than the ones used in the Frio pilot test. Tested rock samples exhibit ductile deformation at in-situ effective stresses. Hence, we do not expect an increase of fault permeability in the Frio sand even in the presence of fault reactivation.

**Keywords:** Carbon geological storage, GOM, dissolution, unconsolidated sand, Frio pilot project, CCS

## 1. Introduction

Pore pressure prediction and management are crucial for successful development and implementation of CO<sub>2</sub> capture and large-scale geological storage. Field evidence shows that the state of stresses in many sedimentary basins is close to limit equilibrium, and therefore the window for pore pressure alteration –without causing geomechanical perturbations– is relatively narrow (Zoback and Gorelick, 2002). High injection rates may trigger open-mode fractures. Large injection volumes even with low injection rate over time can reactivate shear fractures and faults in compartmentalized reservoirs (Bjerrum et al., 1972; Economides and Ehlig-Economides, 2010). Previous studies demonstrate that large-volume injection of water and CO<sub>2</sub> have caused fault reactivation and induced seismicity with magnitude over  $M > 1$  (Frohlich, 2012; Ellsworth, 2013; Bauer et al., 2016). In-depth understanding of short-term implications of pressure build-up and long-term fate of stored CO<sub>2</sub> requires a comprehensive study of (1) petrophysical and geomechanical properties of the target injection formation, (2) caprock, adjacent faults and reservoir compartmentalization, and (3) multiphase and compositional behavior of CO<sub>2</sub> and resident fluids.

Poorly consolidated sediments are good candidates for CO<sub>2</sub> geological storage due to: (1) relatively large porosity and permeability in sandy intervals, (2) high rock compressibility, and (3) ductile deformational behavior. Fault reactivation does not necessarily imply leakage (Rutqvist, 2016). Ductile rocks tend to self-heal in the event of fracturing and subsequent fracture closure. Large sections of the Gulf of Mexico sedimentary basin correspond to this category, including the Frio Formation.

The Frio CO<sub>2</sub> injection pilot project injected about 1,600 metric tons of CO<sub>2</sub> in unconsolidated sands of the Frio Formation at a location near Dayton, Texas. The first injection test targeted the upper Frio Formation (Frio “C” brine-bearing Oligocene age sand) in a fault-bounded formation (Hovorka et al., 2004). The formation is adjacent to a salt dome and is located below the highly heterogeneous Anahuac shale (Figure 1). The injection well was permitted as a Class V underground injection control experimental well with a maximum of 54,000 tons of cumulative injection and a maximum injection rate 250 tons per day (Hovorka et al., 2003). The first pilot test actually injected 1,600 metric tons of CO<sub>2</sub> into the formation for ten days with four main injection and shut-in cycles with approximately constant injection rates of 260 tons per day (Hovorka et al., 2004, 2006; Doughty et al., 2008). The pilot test made use of various monitoring techniques and

tools such as time-lapse well logs, U-tube sampling, and tracer injection test to diagnose and demonstrate the injection progress and CO<sub>2</sub> plume fate (Sakurai et al., 2006). The second Frio pilot project was conducted in 2006 and injected 380 tons of CO<sub>2</sub> into a formation 120 m (360 ft) below the first project injection zone at the same injection rate. Monitoring devices did not detect leakage nor induced seismicity from the Frio injection tests (Hovorka et al., 2006; Doughty et al., 2008). The purpose of this study is to investigate pore pressure build-up induced by CO<sub>2</sub> injection in heterogeneous and compartmentalized poorly consolidated sands. We utilize the Frio pilot CO<sub>2</sub> project as a case study and complement available data with laboratory experiments, well-logging analyses, and reservoir numerical simulations. This article starts with a description of the reservoir model, petrophysical and geomechanical properties, and the compositional phase behavior model. Then, we show the results of history matching for the actual injection schedule and extend conclusions for larger injection volumes and rates. We conclude with an evaluation of expected geomechanical perturbations and limits for injection volumes and rates based on the current in-situ state of stress and flow boundary conditions.

## **2. Frio I Reservoir Model**

### ***2.1 Reservoir Geometry, Boundary Conditions and Simulation Grid***

The detailed area of study (DAS) is a subdomain of interest in the larger Frio reservoir which includes injection and observation wells. The DAS boundaries are determined by faults and a salt dome North-West of the reservoir (Figure 1-a). The reservoir dips 16° towards the South-East. We adopted no-flow boundary conditions for all four boundaries. The lower end of the reservoir is an idealized as an elongated section up to 12 km long (Figure 1-b). Fault 2 and 3 are represented by low permeability planes embedded in the middle of the DAS area. All four faults are normal faults having same strike about N45°W but with different dip angles as interpreted from seismic images and earlier developed models (Hovorka et al., 2006) (Table 1).

The total thickness of the model is 30 m (100 ft) evenly divided into 50 grid blocks of 0.6 m (2 ft) perpendicular to bedding in the x-direction. Parallel to the bedding plane, the model is divided into 78 grid blocks in the y-direction (853 m) and 71 grid blocks in the z-direction (12192 m). The injection zone (approximately 49 m by 61 m (160 ft by 200 ft)) is refined parallel to the bedding (y and z-directions) with 1.5 m (5 ft) grid blocks, and the surrounding area is spaced with gradually

larger sizes of the blocks from 3 m (10 ft) to 305 m (1,000 ft). The full DAS model has 276,900 degrees of freedom. The well injection schedules replicated the field injection/shut-in schedule. Further the initial reservoir pressure was populated using full observation of base pressure at the injection and observation wells.

## 2.2 Petrophysical and Geomechanical Properties of Frio C Sandstone and In-situ Stresses

Frio C sand is composed of subarkosic fine-grained, moderately sorted quartz and feldspar sand grains; with minor amounts of illite, smectite, and calcite (Kharaka et al. 2006). These minor amounts of clay and calcite are located at grain contacts and may affect dynamic elastic properties (Al Hosni et al., 2016). We obtained petrophysical properties from laboratory tests courtesy of GCCC (Gulf Coast Carbon Center, UT Austin) and petrophysical and geomechanical properties from experiments performed in our laboratory. Table 2 summarizes specimen depths and experiments performed.

### 2.2.1 Porosity and Permeability

Experimental measurements as well as well-logging analysis (data courtesy of the GCCC) provided petrophysical properties and geomechanical properties for populating the reservoir model. The well-logging analysis is used to calculate porosity and permeability from data spaced every 0.15 m (0.5 ft). We corrected measured neutron porosity  $\phi_N$  and density porosity  $\phi_D$  for the presence of clays according to Equations (1-2) (Torres-Verdin, 2016).

$$\phi_D^c = \frac{\phi_D - C_{sh}\phi_{D,sh}}{1 - C_{sh}} \quad (1)$$

$$\phi_N^c = \frac{\phi_N - C_{sh}\phi_{N,sh}}{1 - C_{sh}} \quad (2)$$

where  $\phi_D^c$  and  $\phi_N^c$  are shale-corrected density porosity and neutron porosity,  $C_{sh}$  is volumetric concentration of shale, and  $\phi_{D,sh}$  and  $\phi_{N,sh}$  are apparent density porosity and neutron porosity of pure shale. The selected depths for the shale correction are 1516 m (4972.5 ft) for the clay-rich layer (local maximum GR) and 1544 m (5065.5 ft) for the water saturated clay-poor layer (local minimum GR). Table 3 shows the well log GR readings at the two depths. The corrected porosity  $\phi_S^c$  is

$$\phi_S^c = \sqrt{\frac{(\phi_D^c)^2 + (\phi_N^c)^2}{2}} \quad (3)$$

We calculated permeability along the entire injection zone using an empirical correlation between laboratory measured porosity  $\phi$  and permeability  $k$  (Figure 2). Figure 3 shows the resulting corrected porosity and permeability including layers above and below the injection zone. Reservoir properties were averaged from the calculated data; namely the grid block spatial scale is 0.6 m (2 ft) - see Figures 3-a and b for interpolated values of porosity and permeability. We adjusted the ratio between vertical and horizontal permeabilities to 1/3 in order to achieve history matching in the pressure response.

### 2.2.2 Capillary Pressure and Relative Permeability

Capillary pressure measurements suggest that the layered formation can be categorized into different groups of rock depending on the values of the J-function:

$$J(S_w) = \frac{P_c(S_w)}{\gamma \cos \theta} \sqrt{\frac{k}{\phi}} \quad (4)$$

where  $S_w$  is saturation of water,  $P_c$  is capillary pressure,  $\gamma$  is interfacial tension, and  $\theta$  is contact angle (Peters, 2012). We used the J-functions to classify the full reservoir model into four different rock types to build an accurate reservoir model (Table 4). Figure 4-b shows the capillary pressure, and a mapping using converted J-functions from an air-mercury system with interfacial tension at 485 mN/m and contact angle 140° to CO<sub>2</sub>-brine system with interfacial tension 30 mN/m and contact angle 40° (Espinoza and Santamarina, 2010). We employed a Brooks-Corey drainage model to calculate the relative permeability curves from capillary pressure data (Figure 4-b and -c).

$$P_c = P_e (S_w^*)^{-\frac{1}{\lambda}} \quad (5)$$

$$S_w^* = \frac{S_w - S_{wirr}}{1 - S_{wirr}} \quad (6)$$

where  $P_e$  is the capillary entry pressure,  $S_w^*$  is the reduced wetting phase saturation,  $\lambda$  is the pore size distribution index, and  $S_{wirr}$  is irreducible water saturation. The corresponding relative permeabilities are

$$k_{rw}(S_w) = (S_w^*)^{\frac{2+3\lambda}{\lambda}} \quad (7)$$

$$k_{rnw}(S_w) = k_{nrw} \left(1 - \frac{S_w - S_{wirr}}{S_m - S_{wirr}}\right)^2 \left[1 - (S_w^*)^{\frac{2+\lambda}{\lambda}}\right] \quad (8)$$

where  $k_{rw}$  is the relative permeability of wetting phase (brine),  $k_{rnw}$  is the relative permeability of non-wetting phase (CO<sub>2</sub>),  $S_m$  (= 1 for drainage) is the wetting phase saturation corresponding to

the critical non-wetting phase saturation, and  $k_{nwr}$  is the non-wetting phase relative permeability at the irreducible wetting phase saturation. Table 4 lists the modelling parameters used to calculate the relative permeability curves (Figure 4-c). The reservoir model assimilates heterogeneity of capillary pressure and relative permeability as shown in Figure 4-c.

### 2.2.3 Geomechanical Properties

We quantified Frio sand rock compressibility using step loading of pore pressure and confining stress (Bouteca et al., 1999) (Figure 5-a). We saturated sample V1 with synthetic 93,000 ppm salinity NaCl solution as pore fluid and measured volumetric as a function of effective mean stress (Figure 5-b). The corresponding bulk rock compressibility is  $4.6 \cdot 10^{-8} \text{ MPa}^{-1}$  ( $6.3 \cdot 10^{-6} \text{ psi}^{-1}$ ) evaluated using the following equations assuming negligible mineral compressibility

$$C_p = \frac{1}{V_p} \frac{\Delta V_p}{\Delta P_p} = \frac{\Delta \varepsilon_{vol}}{\Delta P_p} \quad (9)$$

Calculated rock compressibility was taken to be constant throughout the reservoir.

We also conducted a multistage deviatoric loading test to evaluate strength and post-peak failure behavior of the Frio C sand. The multistage loading consisted of increasing deviatoric stress at three different constant confining stresses: 3.4 MPa (500 psi), 6.9 MPa (1,000 psi), and 10.3 MPa (1,500 psi) (Figure 6-a). During the first two loading stages, the sample exhibited dilative behavior by increasing deviatoric stress. Finally, shear yield was allowed at the last loading stage. The sand resulting friction angle is about  $38^\circ$ , and the cohesive strength is zero (Figure 6-b). The sand undergoes ductile deformation at peak stress.

### 2.2.4 In-situ Stresses

We estimated the magnitude and direction of principal stresses using an overburden (total vertical stress) gradient of 20.5 MPa/km (0.907 psi/ft) (Hovorka et al., 2003) and considered the effect of the rising salt dome on “dome hoop stresses” (minimum principal stress oriented in circumferential direction - Nikolinakou et al., 2014). We assumed a limit frictional equilibrium of the sand unit (Zoback, 2007) (friction angle from Section 2.2) and a normal faulting regime from the seismic interpretation of strikes and dips of the respective faults (Figure 1). At limit frictional equilibrium between vertical and horizontal stress, the friction angle dictates the vertical-to-horizontal effective stress anisotropy:

$$\frac{\sigma_1}{\sigma_3} = \frac{S_v - P_p}{S_{hmin} - P_p} \leq \frac{1 + \sin(\varphi)}{1 - \sin(\varphi)} \quad (10)$$

where  $\sigma_1$  and  $\sigma_3$  are maximum and minimum principal effective stress  $\varphi$  is the friction angle,  $S_v$  is the total vertical stress,  $S_{hmin}$  is the minimum total horizontal stress, and  $P_p$  is the pore pressure. At the perforation depth of the injection well, measured bottomhole pressure  $P_p$  was 14.8 MPa (2153 psi), and calculated  $S_v$  was 31.6 MPa (4580.4 psi). Using  $\varphi = 38^\circ$  (Figure 6), limit frictional equilibrium provides an estimate of the lower bound of minimum principal stress (horizontal) around the injection zone. This value was estimated to be 18.8 MPa (2,734 psi).

Stress anisotropy may decrease with time due to creep. Hovorka et al. (2003) calculated formation fracture pressure equal to 26.6 MPa (3,851 psi) at a depth of 1,667 m (5,000 ft) based on Eaton's equation using Poisson's ratio  $\nu = 0.416$ , overburden gradient 0.907 psi/ft, and reservoir pressure gradient 0.432 psi/ft.

$$S_{hmin} = \left(\frac{\nu}{1-\nu}\right) (S_v - P_p) + P_p \quad (11).$$

## 2.3 Reservoir Simulator

### 2.3.1 Simulation Methodology

The compositional flow model in IPARS uses the Peng-Robinson cubic equation of state (PR-EOS) for describing fluid phase behavior. The conservation equations for each component (Equations 12-13) are discretized in time using the backward Euler scheme resulting in a fully implicit system in pressure and concentration unknowns. A lowest order mixed finite element method (equivalent to cell-centered finite differences) was used for the spatial discretization. The component concentration equations can be written as,

$$\frac{\partial}{\partial t} (\phi N_i) + \nabla \cdot F_i - \nabla \cdot \left( \sum_{\alpha} \phi S_{\alpha} D_{i\alpha} (\nabla \rho_{\alpha} x_{i\alpha}) \right) = q_i \quad (12)$$

$$F_i = -K \Lambda_i \left( \nabla P_{ref} - \frac{1}{\Lambda_i} \sum_{\alpha} \rho_{\alpha} x_{i\alpha} \frac{k_{r\alpha}}{\mu_{\alpha}} \rho_{m,\alpha} g + \frac{1}{\Lambda_i} \sum_{\alpha \neq ref} \rho_{\alpha} x_{i\alpha} \frac{k_{r\alpha}}{\mu_{\alpha}} \nabla P_{c\alpha} \right) \quad (13)$$

where  $\Lambda_i = \sum_{\alpha} \rho_{\alpha} x_{i\alpha} \frac{k_{r\alpha}}{\mu_{\alpha}}$  is the mobility,  $N_i = \sum_{\alpha} \rho_{\alpha} S_{\alpha} x_{i\alpha}$  is the concentration,  $q_i = \sum_{\alpha} q_{i\alpha}$  is the injection/production rate, and  $F_i$  is the flux of component  $i$ . Further  $S_{\alpha}$  is saturation of phase  $\alpha$ ,  $D_{i\alpha}$  is diffusion coefficient,  $x_{i\alpha}$  is mole fraction of component  $i$  in phase  $\alpha$ ,  $K$  is permeability tensor,  $P_{ref}$  is reference pressure,  $\rho_{m,\alpha}$  is mass density, and  $P_{c\alpha}$  is capillary pressure of phase  $\alpha$  (Singh and Wheeler, 2016). The phase equilibrium is calculated using the Rachford-Rice equation (Rachford-Rice, 1952) and iso-fugacity criteria. Further details regarding the compositional flow formulation, phase behavior model, and numerical solution scheme can be found in Singh and Wheeler (2016).

IPARS compositional flow module has been used extensively for evaluating various sequestration and gas injection scenarios (Delshad et al., 2011; Kong et al., 2015). Although PR-EOS is developed for non-polar molecules such as hydrocarbons, IPARS allows water phase properties to be calculated using PR-EOS. This is achieved by modifying the binary interaction parameters (BIP) for the components. In this study, we tuned the BIPs of the PR-EOS to match experimentally observed solubility of CO<sub>2</sub> in brine. Table 5 shows the EOS parameters used in this study. The calculations further assume CO<sub>2</sub> and brine as chemical components wherein the CO<sub>2</sub> component can exist in both gaseous and aqueous phases. The brine component is considered to exist only in the liquid phase. We considered two approaches for studying CO<sub>2</sub> migration (discussed in detail in Section 3.4). The miscible case uses PR-EOS for calculating both gas and aqueous phase properties. The immiscible case uses PR-EOS and slightly compressible approach for gas and aqueous phase, respectively.

A tensor product refinement was used to capture the DAS, where the injection and observation wells are located. This allowed us to assimilate detailed rock property data from well logs such as permeability, porosity, as discussed before. This approach is especially useful when limited amount of reservoir properties are available from well logs, seismic observations and geological models. Although the numerical simulation model used tensor product refinements, present IPARS capabilities allow computationally efficient local adaptive mesh refinement for long term evaluation of multiple sequestration scenarios.

### 2.3.2 Simulation Description

Reservoir simulation included various cases (Table 6):

- Baseline scenario: history match case (BC)
- Sensitivity analysis cases varying injection rates (IR)
- Immiscible flooding case to compare with baseline scenario (IM).

We performed history matching with the model described in Sections 2.1 and 2.2. The initial pressure was determined using equilibrium calculation as preprocessing step. The binary interaction coefficient for brine and CO<sub>2</sub> ( $BIC_{H_2O-CO_2}$ ) interaction was evaluated according to the relationship introduced by Kong et al. (2013),

$$BIC_{H_2O-CO_2} = -0.093625 + [4.861 \cdot 10^{-4}(T - 113)] + (2.29 \cdot 10^{-7}S) \quad (14)$$

where T is temperature (°F), and S is salinity (ppm). The binary coefficient was calculated to be -

0.06212 at a reservoir, temperature of 134 °F (56.7 °C) and brine salinity of 93,000 ppm.

The objective of CO<sub>2</sub> injection simulations was to quantify the maximum injection volume required for the fluid pressure to reactivate faults or fracture the injector. We examined the effect of CO<sub>2</sub> solubility on pore pressure build-up computing the immiscible and miscible scenario described above.

### **3. Results and Discussion**

#### ***3.1 History-Match***

Figure 7 shows history-matching of pressure responses for four injection cycles in the base case, including injection and shut-in periods for both the injection and observation wells. The pressure response in the first injection cycle does not coincide with simulation results. This peak might have occurred due to effects of formation damage or near-wellbore perforation complexity. However, the CO<sub>2</sub> breakthrough time was predicted by numerical simulation to be 2.3 days as compared to 2.1 days observed in field.

Figure 8 shows snapshots of the CO<sub>2</sub> plume migration up to 60 days after injection. The CO<sub>2</sub> plume moves toward the observation well due to buoyancy but does not go through low permeability layers. Figure 8-a shows the total CO<sub>2</sub> concentration (CO<sub>2</sub> [lb-mole]/pore volume [ft<sup>3</sup>]) in both gas phase and dissolved phase while Figure 8-b shows CO<sub>2</sub> saturation of the gas phase only (bulk supercritical CO<sub>2</sub>). Initially, the two figures show similar CO<sub>2</sub> saturation distribution since the CO<sub>2</sub> has not dissolved extensively into brine yet. After 30 days of the injection, the difference between Figures 8-a and -b demonstrates a considerable amount of dissolved CO<sub>2</sub> around injection zone (approximately 30%).

Rock compressibility  $C_p$  is one of the key mechanical properties determining pore pressure build-up. Rock compressibility lowers the pore pressure buildup at the injection well by increasing available pore volume. Zero rock compressibility results in a steady increase of wellbore pressure for rate specified injection well. In fact the pressure buildup is twice for zero rock compressibility compared to the field observations at both injection and observation wells. The simulation results show flattening pressure transient curve during constant injection rate using the rock compressibility estimated from the laboratory.

### 3.2 Injection Rate to Induce Fault Reactivation

This section applied results of reservoir simulation to determine critical pore pressures and injection rates for fault reactivation. Normal and shear stresses are calculated at four faults from the estimated principal stresses in Section 2.2.4. The stress tensor in geographical coordinates  $S_g$  is obtained by applying a transformation matrix  $R_1$  to the principal stress tensor.

$$S_g = R_1^T S R_1 = R_1^T \begin{bmatrix} S_1 & 0 & 0 \\ 0 & S_2 & 0 \\ 0 & 0 & S_3 \end{bmatrix} R_1 \quad (15),$$

where

$$R_1 = \begin{bmatrix} \cos a \cos b & \sin a \cos b & -\sin b \\ \cos a \sin b \sin c - \sin a \cos c & \sin a \sin b \sin c + \cos a \cos c & \cos b \sin c \\ \cos a \sin b \cos c + \sin a \sin c & \sin a \sin b \cos c - \cos a \sin c & \cos b \cos c \end{bmatrix} \quad (16),$$

and Euler rotation angles  $a = 44.85^\circ$ ,  $b = 90^\circ$ , and  $c = 0^\circ$  for the location shown in Figure 1 (Zoback, 2007). Then, we calculate the magnitudes of shear stress  $\tau$  and normal stress  $S_n$  on the fault plane from the projection of  $S_g$ , using the respective fault strikes and dip transformation vectors  $n_n$  and  $n_d$ , (function of fault strike  $str$  and dip  $dip$ ).

$$\tau = \{S_g[n_n]\}^T n_d = \left\{ S_g \begin{bmatrix} -\sin(str) \sin(dip) \\ \cos(str) \sin(dip) \\ -\cos(dip) \end{bmatrix} \right\}^T \begin{bmatrix} -\sin(str) \cos(dip) \\ \cos(str) \cos(dip) \\ \sin(dip) \end{bmatrix} \quad (17),$$

$$S_n = \{S_g[n_n]\}^T n_n = \left\{ S_g \begin{bmatrix} -\sin(str) \sin(dip) \\ \cos(str) \sin(dip) \\ -\cos(dip) \end{bmatrix} \right\}^T \begin{bmatrix} -\sin(str) \sin(dip) \\ \cos(str) \sin(dip) \\ -\cos(dip) \end{bmatrix} \quad (18),$$

Figure 9 shows the stress conditions at each fault at initial pore pressure condition before the injection assuming a non-zero cohesive strength in the rock matrix. The values of principal stresses change depending on the depth. The value of principal stresses at the injection well is specified in Section 2.2.4. As pore pressure increases, the effective normal stress on the fault plane decreases and the Mohr circle moves towards the yield line increasing the possibility of the shear yield at the fault plane.

Figure 10 shows the maximum amount of CO<sub>2</sub> injection without causing fault reactivation as a function of injection rate. The maximum cumulative amount of CO<sub>2</sub> injection is about 130,000 tons, and it is relatively dependent of injection rates – for low injection rates. The first location of fault reactivation (Fault 2) is observed for all injection rate cases (Table 7). Extremely high

injection rates over 10,000 tons/day may fracture the well before causing fault reactivation.

Overall, the results indicate that the first Frio pilot test injected less than 1.6% of the minimum possible amount of CO<sub>2</sub> storage without perturbing faults (Figure 10). Assumption of negligible rock compressibility results in a reduction of storage capacity by a factor of ten. These values are provided as an illustrative comparison for compartmentalized reservoirs in formations near the limit of stress equilibrium. Actual predictions need to measure in-situ stress magnitude and orientation and should account for flow boundary conditions that may allow for leaks at faults.

Tertiary unconsolidated sands and mudrocks at Frio do not exhibit brittle deformation during shearing. Figure 6-a shows slight strain hardening behavior of Frio sand at in-situ effective stresses. Large induced seismicity events and failure localization (and local increases in permeability) are less likely to occur in geological formations that sustain large plastic strains at yield.

### ***3.3 Injection Rate to Induce Open-Mode Fractures***

Figure 10 summarizes simulation results showing the maximum amounts of CO<sub>2</sub> injection needed to fracture the injection well (assuming that bottom hole pressure reaches the minimum principal stress) and zero fault leakage upon reactivation. If faults are leaky, then an open-mode fracture may not develop due to the pore pressure control at faults. Fault reactivation predates hydraulic fracturing for typical injection rates < 10,000 ton per day. Injection rates above 10,000 tons per day can cause hydraulic fracturing before fault reactivation and are not affected by domain size because of the sharp pressure gradient developed around the injection wellbore (Table 7). Hovorka et al. (2003) suggested a maximum injection rate of 250 tons per day. Injection pressure and rate used at the first Frio pilot test seems to be significantly below thresholds for developing open-mode fractures.

### ***3.4 Pore Pressure Reduction Due to CO<sub>2</sub> Dissolution into Brine***

Immiscible two-phase fluid flow simulation (Simulation IM) shows 75.9 kPa (11 psi) higher pressure response compared to compositional Simulation BC due to no dissolution of CO<sub>2</sub> into the brine (Figure 7). The amount of dissolved CO<sub>2</sub> in Simulation BC increases with time as the plume spreads in the brine-saturated reservoir. The binary interaction coefficient, one of the key parameters of CO<sub>2</sub> solubility in brine, has large effects on the pore pressure for a given injection scenario. At the end of injection, approximately 20% of the CO<sub>2</sub> was dissolved in the brine. After

20 days of the end of injection, 44% of the injected CO<sub>2</sub> was dissolved into the brine, and eventually, 91% of the CO<sub>2</sub> was dissolved after 95 days (Figure 8). The CO<sub>2</sub> plume in immiscible simulation (IM) is thinner and moves faster than that in simulation using BC. Results indicate that CO<sub>2</sub> dissolution contributes a fair proportion to trapping for small CO<sub>2</sub> injection volumes. CO<sub>2</sub> dissolution in the brine phase alleviates pore pressure buildup and extends injection times without effecting mechanical stability compared to the immiscible case. We predict that injection can be carried out for an additional two days at 200 tons per day. The effect of dissolution on pore pressure buildup is stronger in rocks with low pore compressibility.

#### **4. Conclusions**

In this study, we investigated the geomechanical implications of injecting CO<sub>2</sub> in a fault-bounded reservoir comprised by tertiary sediments. We used the Frio pilot CO<sub>2</sub> sequestration project as a case study and matched field data. We also predicted long term storage study feasibility for the Frio formation using numerical simulation. The history-matched simulation was used as the base case to conduct injection rate sensitivity studies to predict thresholds for geomechanical perturbations. Simulations results show that:

- The history-matched simulation shows a considerable amount of dissolved CO<sub>2</sub> in brine for a hundred days after the injection was completed. CO<sub>2</sub> dissolution into brine reduce tens-of-psi pore pressure buildup and resulting in 91% trapping after 95 days for an injection of 1,600 tons of CO<sub>2</sub> in the first Frio pilot project.
- Simulations using a large range of injection rates show that fault reactivation is likely to occur after the injection of about 100,000 tons assuming a closed compartment model (sixty times of the amount injected at the first Frio Pilot project). The actual amount of injection for fault reactivation would depend on accurately determined in-situ stresses and flow boundary conditions. Storage volume decreases with injection rate following a power law relationship.
- High reservoir permeability, high rock/pore compressibility, and low CO<sub>2</sub> viscosity render hydraulic fracturing of the injector unlikely. Pore pressure build-up transfers quickly to neighboring faults for injection rates smaller than ~10,000 tons per day.
- The deformational behavior of the tested unconsolidated sediments at yield shear stresses tends to be ductile rather than brittle and may not create significant seismic events or

localize channels of high permeability upon fault reactivation.

## Acknowledgements

Financial support for this research was provided by the Department of Energy of the United States of America (DOE-NETL) through grant number DE-FE0023314. The authors are thankful to Susan Hovorka, Seyyed Hosseini, and Tip Meckel of the Gulf Coast Carbon Center at the Bureau of Economic Geology (The University of Texas at Austin) for sharing field data and thoughtful discussions. The Texas Advanced Computing Center provided additional computational resources.

## References

- Bjerrum, L., Kennard, R. M., Gibson, R. E., and Nash, J. 1972. Hydraulic fracturing in field permeability testing. *Geotechnique*, Vol. 22, Iss. 2, pp. 319-332.  
<http://dx.doi.org/10.1680/geot.1972.22.2.319>
- Bauer, S. J., Huang, K., Chen, Q., Ghassemi, A., and Barrow, P. 2016. Experimental and Numerical Investigation of Hydro-Thermally Induced Shear Stimulation. 50 U.S. Rock Mechanics/Geomechanics Symposium, Houston, Texas, 26-29 June.
- Delshad, M., Kong, X., & Wheeler, M. F. 2011. On Interplay of Capillary, Gravity, and Viscous Forces on Brine/CO<sub>2</sub> Relative Permeability in a Compositional and Parallel Simulation Framework. Presented at the SPE Reservoir Simulation Symposium, The Woodlands, Texas, 21-23 February. SPE-142146-MS.  
<http://dx.doi.org/10.2118/142146-MS>
- Delshad, M., Thomas, S. G. and Wheeler, M. F. 2011. Parallel Numerical Reservoir Simulations of Nonisothermal Compositional Flow and Chemistry. *Society of Petroleum Engineers*, 118847-PA, Vol. 16, Iss. 2. pp 239-248.  
<http://dx.doi.org/10.2118/118847-PA>
- Doughty, C., Freifeld, B. M., Trautz, R. C. 2008. Site characterization for CO<sub>2</sub> geologic storage and vice versa: the Frio brine pilot, Texas, USA as a case study. *Environmental Geology*, Vol. 54, Iss 8, pp. 1635-1656.  
<http://dx.doi.org/10.1007/s00254-007-0942-0>
- Ehlig-Economides, C. and Economides, M. J. 2010. Sequestering carbon dioxide in a closed underground volume. *Journal of Petroleum Science and Engineering*, Vol. 70, Iss 1-2, pp. 123-130.  
<http://dx.doi.org/10.1016/j.petrol.2009.11.002>
- Ellsworth, W. L. 2013. Injection-Induced Earthquakes. *Science*, Vol. 341 Iss 6142, pp 1225942  
<http://dx.doi.org/10.1126/science.1225942>
- Espinoza, D. N., and Santamarina J. C. 2010. Water-CO<sub>2</sub>-mineral systems: Interfacial tension, contact angle, and diffusion—Implications to CO<sub>2</sub> geological storage, *Water Resources Research*, Vol. 46, Iss. 7, pp. 1-10.  
<http://dx.doi.org/10.1029/2009WR008634>
- Frohlich, C. 2012. Two-year survey comparing earthquake activity and injection-well locations in the Barnett Shale, Texas, *Proceedings of the National Academy of Sciences of the United States of America*, Vol. 109, Iss 35, pp 13934-13938

- <http://dx.doi.org/10.1073/pnas.1207728109>
- Hovorka, S. D., Holtz, M. H., Sakurai, S., and others 2003. Report to the Texas Commission on Environmental Quality to Accompany a Class V Application for an Experimental Technology Pilot Injection Well: Frio Pilot in CO<sub>2</sub> Sequestration in Brine-Bearing Sandstones.  
[http://www.beg.utexas.edu/gccc/pubs\\_presentations/friopilotapplication.pdf](http://www.beg.utexas.edu/gccc/pubs_presentations/friopilotapplication.pdf)
- Hovorka, S. D., Doughty, C., Benson, S. M., Pruess, K., and Knox, P. R. 2004. The impact of geological heterogeneity on CO<sub>2</sub> storage in brine formations: a case study from the Texas Gulf Coast. *Geological Society*, London, Special Publications, Vol. 233, pp. 147-163.  
<http://dx.doi.org/10.1144/GSL.SP.2004.233.01.10>
- Hovorka, S. D., C. Doughty, S. M. Benson, and others 2006. Measuring permanence of CO<sub>2</sub> storage in saline formations: The Frio experiment. *Environmental Geosciences*, Vol. 13, Iss. 2., pp. 105–121.  
<http://dx.doi.org/10.1306/eg.11210505011>
- Kharaka, Y. K., Cole, D. R., Hovorka, S. D., and others 2006. Gas-water-rock interactions in Frio Formation following CO<sub>2</sub> injection: Implications for the storage of greenhouse gases in sedimentary basins. *Geology*, Vol. 34, Iss. 7, pp. 577-580.  
<http://dx.doi.org/10.1130/G22357.1>
- Kim, J., Tchelepi, H. A., Juanes, R. 2011. Stability, accuracy, and efficiency of sequential methods for coupled flow and geomechanics. *Society of Petroleum Engineers*, Vol. 16, Iss. 02, pp 249-262.  
<http://dx.doi.org/10.2118/119084-PA>
- Kong, X., Delshad, M., and Wheeler, M. F. 2015. History Matching Heterogeneous Coreflood of CO<sub>2</sub>/brine by Use of Compositional Reservoir Simulator and Geostatistical Approach. *Society of Petroleum Engineers*, Vol. 20, Iss. 2, 267-276.  
<http://dx.doi.org/10.2118/119084-PA>
- Nikolinakou, M. A., Flemings, P. B., and Hudec, M. R. 2013. Modeling stress evolution around a rising salt diapir. *Marine and Petroleum Geology*, Vol. 51, pp. 230-238.  
<http://dx.doi.org/10.1016/j.marpetgeo.2013.11.021>
- Mikelic, A. and Wheeler, M. F. 2013. Convergence of iterative coupling for coupled flow and geomechanics. *Computational Geosciences*, Vol. 17, Iss. 03, pp 455-461.  
<http://dx.doi.org/10.1007/s10596-012-9318-y>
- Peters, E. J. 2012, *Advanced Petrophysics*. Austin, Texas: Live Oak Book Company
- Rachford, H.H., Rice, J.D. 1952. Procedure for the use of electronic digital computers in calculating flash vaporization hydrocarbon equilibrium. *Society of Petroleum Engineers*. Vol. 4, Iss 10, pp 327-328  
<http://doi.org/10.2118/952327-G>
- Rutqvist, J., Rinaldi, A. P., Cappa, F., Jeanne, P., Mazzoldi, A., Urpi, L., Guglielmi Y. & Vilarrasa, V. (2016). Fault activation and induced seismicity in geological carbon storage—Lessons learned from recent modeling studies. *Journal of Rock Mechanics and Geotechnical Engineering*, Vol. 8, Iss 6, pp 789-804  
<https://doi.org/10.1016/j.jrmge.2016.09.001>
- Sakurai, S., Ramakrishnan, T. S., Boyd, A., Mueller, N., and Hovorka, S. D. 2006. Monitoring Saturation Changes for CO<sub>2</sub> Sequestration: Petrophysical Support of the Frio Brine Pilot Experiment. *Society of Petrophysics and Well Log Analysis*, Vol. 47, Iss. 6, pp. 483-496.
- Settari, A. and Maurits, F. 1998. A coupled reservoir and geomechanical simulations system. *Society of Petroleum Engineers*, Vol. 3, Iss. 2, pp. 219-226.

<http://dx.doi.org/10.2118/50939-PA>

Singh, G. and Wheeler, M. F. 2016. Compositional Flow Modeling using a Multipoint Flux Mixed Finite Element Method. *Computational Geosciences*, Vol. 20, pp. 421-435.

<http://dx.doi.org/10.1007/s10596-015-9535-2>

Torres-Verdin, C. 2016. Integrated Geological-Petrophysical Interpretation of Well Logs. Course Notes of Fundamentals of Well Logging, The University of Texas at Austin

Wheeler, J.A., Wheeler, M.F. and Yotov, I. 2002. Enhanced Velocity Mixed Finite Element Methods for Flow in Multiblock Domain. *Computational Geosciences*, Vol. 6, Iss. 3, pp 315-332.

<http://dx.doi.org/10.1023/A:1021270509932>

Zoback, M. D. and Gorelick, S. M. 2012. Earthquake triggering and large-scale geologic storage of carbon dioxide. *Proceedings of the National Academy of Sciences*, Vol. 109, Iss. 26, pp. 10164-10168

<http://dx.doi.org/10.1073/pnas.1202473109>

Zoback, M. D. 2007. Reservoir geomechanics. Cambridge: Cambridge University Press.

## Tables

Table 1. Information about faults in DAS

	Depth (closest to injection well)	Strike	Dip
Fault 1	1,566 m (5,139 ft)	N45°W	87°NE
Fault 2	1,542 m (5,060 ft)	N45°W	77°NE
Fault 3	1,458 m (4,873 ft)	N45°W	77°NE
Fault 4	1,408 m (4,621 ft)	N45°W	78°NE

Table 2. Information of samples from laboratory experiments

Depth [ft]	Depth [m]	Plug direction	Type of experiments	Porosity [-]	Permeability [mD]
5051.8	1539.8	Horizontal	Gas permeability, MICP (GCCC)	0.308	837
5050.4	1539.3	Horizontal	Gas permeability, MICP (GCCC)	0.277	25
5051.2	1539.6	Horizontal	Gas permeability, MICP (GCCC)	0.244	45
5053.4	1540.3	Horizontal	Gas permeability, MICP (GCCC)	0.326	2930
5055.1	1540.8	Vertical (V1)	Multistage triaxial loading, N <sub>2</sub> -brine injection at in-situ stress condition (Biot coefficient and compressibility), MICP (Our laboratory)	0.376	263
5055.8	1541.0	Horizontal (H1)	Porous plate capillary pressure measurement (Our laboratory)	0.377	-
5055.9	1541.0	Vertical (V2)	Porous plate capillary pressure measurement (Our laboratory)	0.355	-
5061.4	1542.7	Horizontal	Gas permeability, MICP (GCCC)	0.331	1150
5065.6	1544.0	Horizontal	Gas permeability, MICP (GCCC)	0.327	1830
5070.5	1545.5	Horizontal	Gas permeability, MICP (GCCC)	0.280	212
5071.5	1545.8	Horizontal	Gas permeability, MICP (GCCC)	0.353	2650
5075.4	1547.0	Horizontal	Gas permeability, MICP (GCCC)	0.326	1080
5076.3	1547.3	Horizontal	Gas permeability, MICP (GCCC)	0.340	2330

Table 3. Measured well log values at depths for shale correction

Property	Water saturated sands	Clay-rich sands
Depth [m]	1,544 m (5065.5 ft)	4,972.5
Gamma ray [GAPI]	45.5	148.9
Density porosity $\phi_{D,sh}$ [-]	0.354	0.260
Neutron porosity $\phi_{N,sh}$ [-]	0.348	0.501

Table 4. Rock types applied to Frio reservoir modeling for capillary pressure and relative permeability. (Assumed parameters include  $k_{rnw} = 0.82$  and  $S_m = 1$ )

Property	Tight	Medium	Coarse 1	Coarse 2
Permeability [mD]	0.3	618	1026	2107
Porosity [-]	0.1	0.24	0.29	0.36
J-function	1	2	3	3
$\lambda$	0.29	1.1	2	1.9
$P_e$ [MPa]	0.0055	0.0021	0.0028	0.0016
$S_{wirr}$	0.5	0.279	0.263	0.263

Table 5. EOS parameters for CO<sub>2</sub> and brine flow calculation.

	$T_c$ [R°]	$P_c$ [psi]	$Z_c$	$\omega$ [-]	$M_w$ [g/mol]	$P$ [-]	$V_{shift}$ [-]	BIC
<b>CO<sub>2</sub></b>	547.56	1070.38	0.3023	0.2240	44.01	78.0	0.0247	-0.0602
<b>Brine</b>	1165.23	3203.88	0.2298	0.2240	19.35	52.0	0.2340	-0.0602

Table 6. Simulation input settings varied in simulations.

	BC	IM	IR1	IR2	IR3	IR4	IR5	IR6	IR7	IR8
<b>Miscible/ Immiscible flow</b>	Miscible	Immiscible					Miscible			
<b>Injection rate (ton/day)</b>	Field data	Field data	200	500	1,000	2,000	5,000	10,000	20,000	30,000

Table 7. Pore pressure at injection well and nearby faults for different injection rates (constant) and elapsed time to reach fault reactivation (marked with \*) with closed boundary. Injector fracturing is marked with \*\*.

Injection rate (ton/day)	Time after beginning of injection (days)	Pore pressure at injection well and faults [MPa]				
		Injection well	Fault 1	Fault 2	Fault 3	Fault 4
<b>200</b>	650	15.8	16.0	15.3*	14.5	14.3
<b>500</b>	113	15.9	16.1	15.3*	14.5	14.3
<b>1,000</b>	36	16.0	16.1	15.3*	14.4	14.2
<b>2,000</b>	12	16.2	16.2	15.3*	14.3	14.1
<b>5,000</b>	3.05	16.7	16.5	15.3*	14.1	13.8
<b>10,000</b>	1.1	17.5	16.9	15.3*	13.8	13.6
<b>20,000</b>	0.5	18.5**	17.2	15.3*	13.5	13.3
<b>30,000</b>	0.19	20.3**	18.0	15.3*	13.4	13.3

## Figures

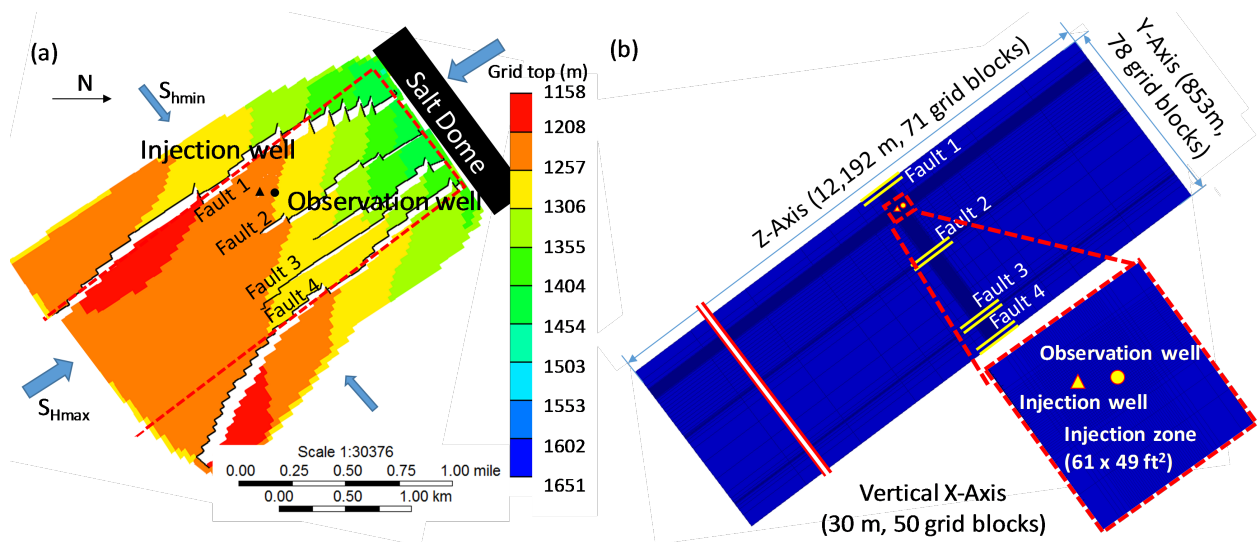


Figure 1. (a) Schematic diagram of Frio structure (Top view). The dashed red box is the selected region for building a DAS reservoir. (b) Detailed area of study reservoir model geometry and zoom-in into the grid refinement around the injection zone. Double-yellow lines show the faults locations analyzed in this study.

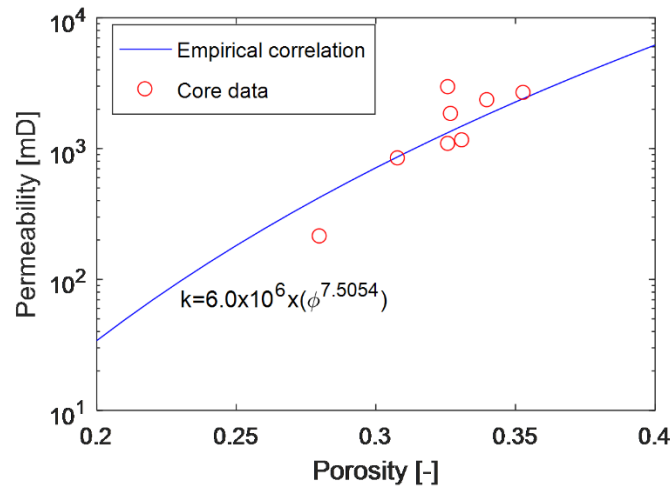


Figure 2. Porosity and permeability empirical relationship from core measurements.

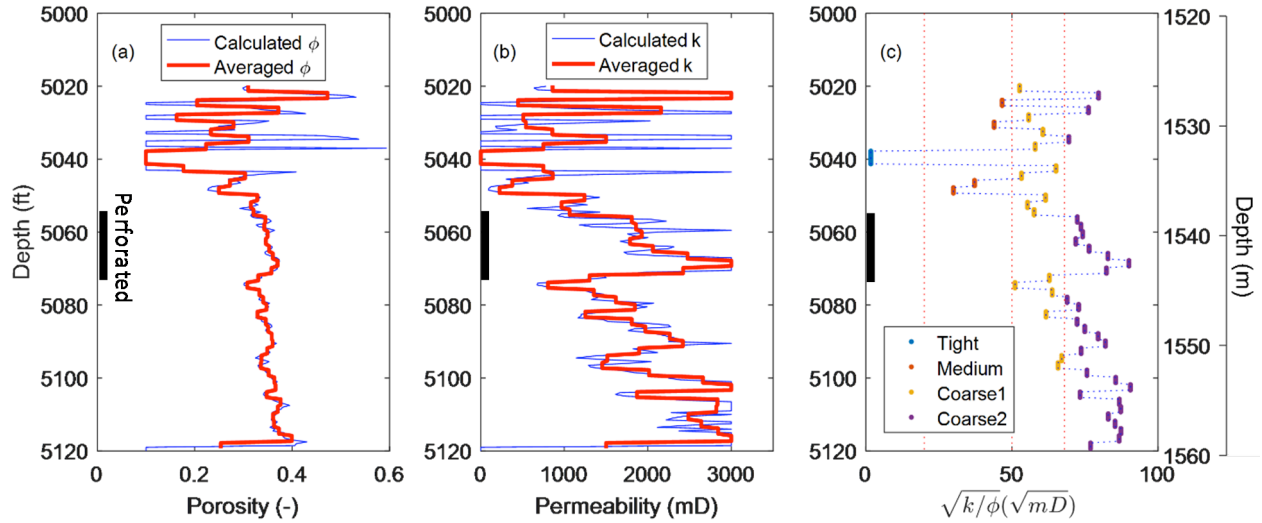


Figure 3. (a) Porosity, (b) permeability, and (c) ratio  $\sqrt{k/\phi}$  around the injection well as a function of measured depth: calculated from well-logs (blue line), adopted in model (red line).

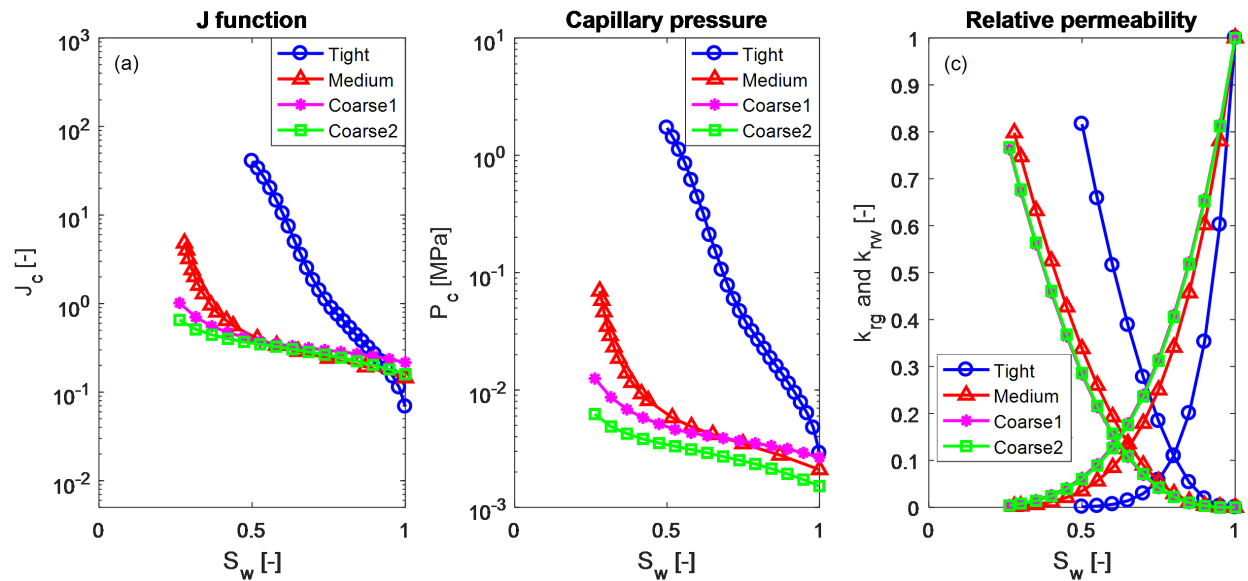


Figure 4. (a) J-function, (b) capillary pressure, and (c) relative permeability of four rock types assimilated into the reservoir model.

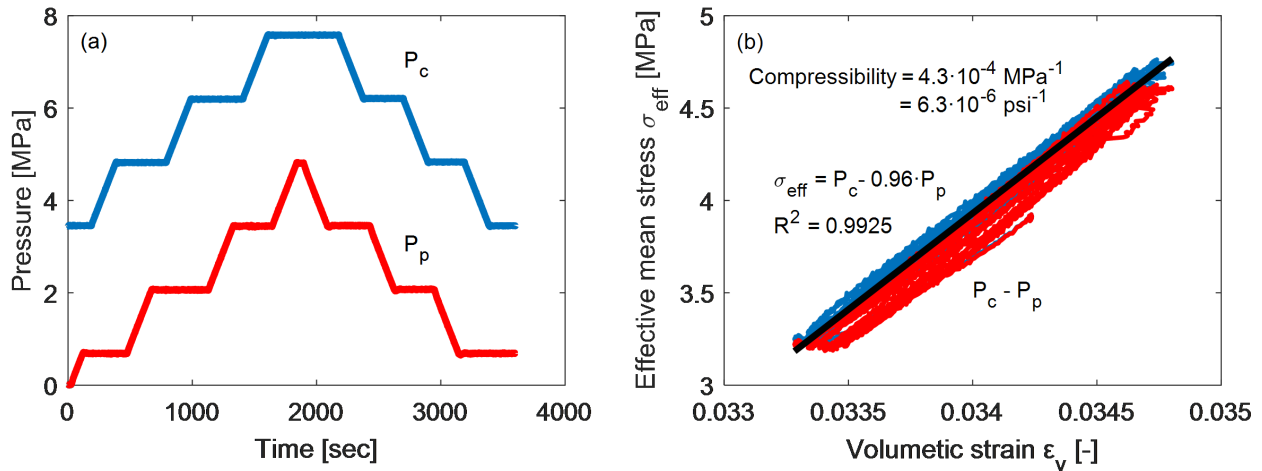


Figure 5. Results of pore pressure and confining stress loading and unloading on Frio sand: (a) loading paths of pore pressure  $P_p$  and confining stress  $P_c$  (b) volumetric stress change as a function of effective mean stress. The resulting Biot coefficient is 0.96.

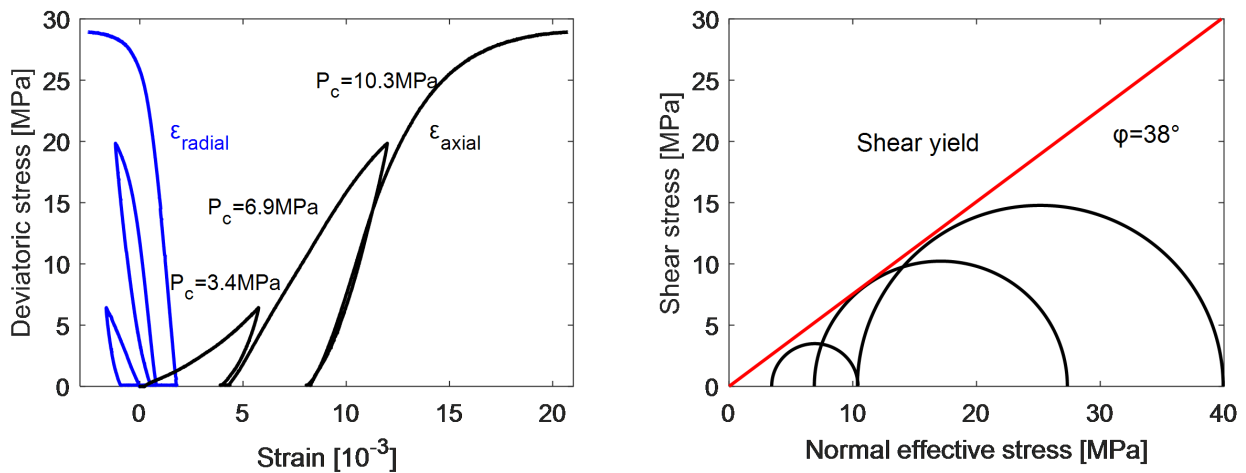


Figure 6. Results of multistage triaxial loading on Frio sand at confining stress 3.4 MPa, 6.9 MPa and 10.3 MPa: (a) deviatoric stress as a function of axial and radial strains and (b) Mohr-Coulomb shear yield line.

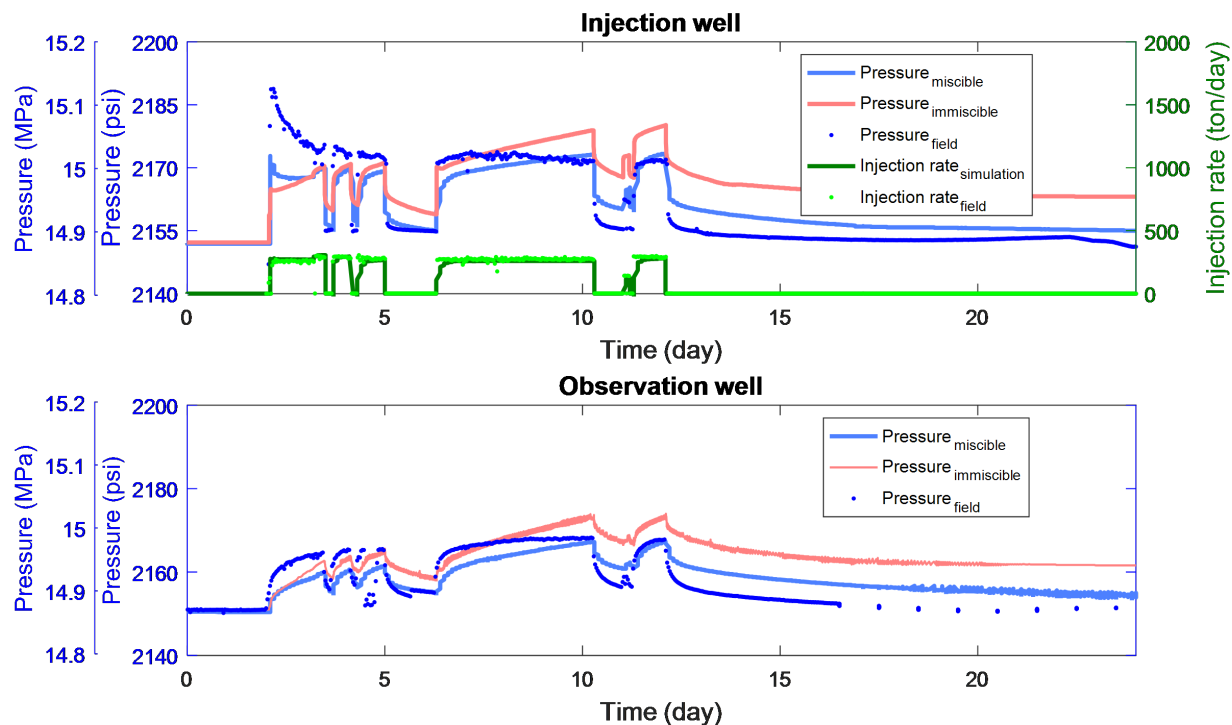


Figure 7. Injection rate and the bottom-hole pressure response at the injection well of Frio field and history matched simulation results.

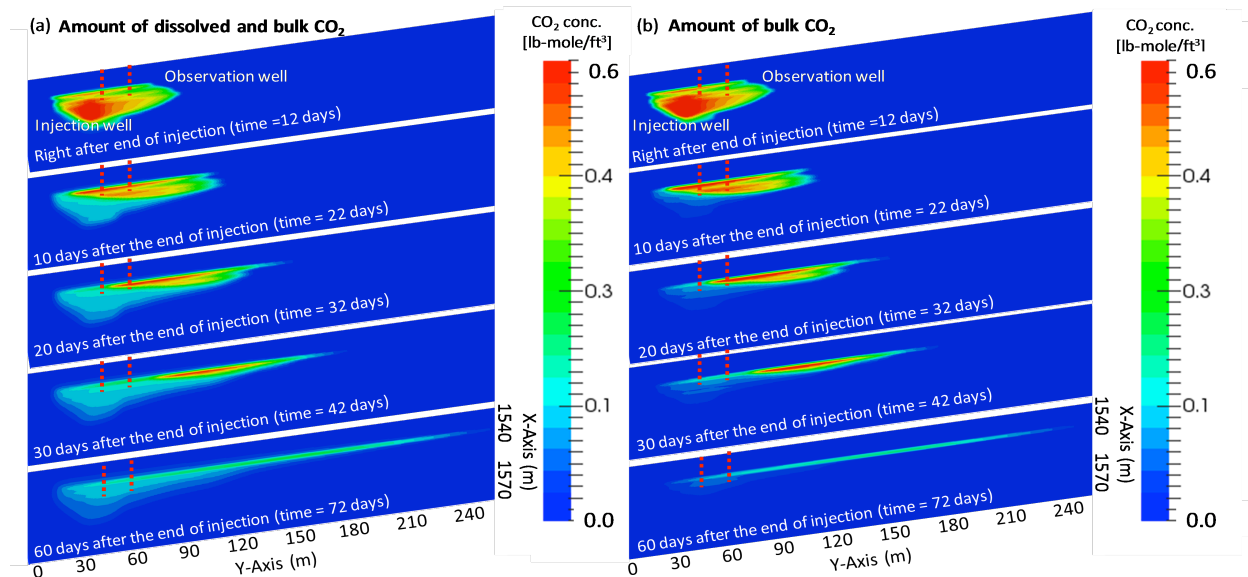


Figure 8. History-matched simulation: (a) CO<sub>2</sub> amount in bulk conditions and dissolved, and (b) CO<sub>2</sub> amount in bulk conditions along a cross section passing by the injection and observation wells. Dissolution amounts (total minus bulk) are  $< \sim 0.1$  lb-mole/ft<sup>3</sup> CO<sub>2</sub> = 1.6 mole/L CO<sub>2</sub>.

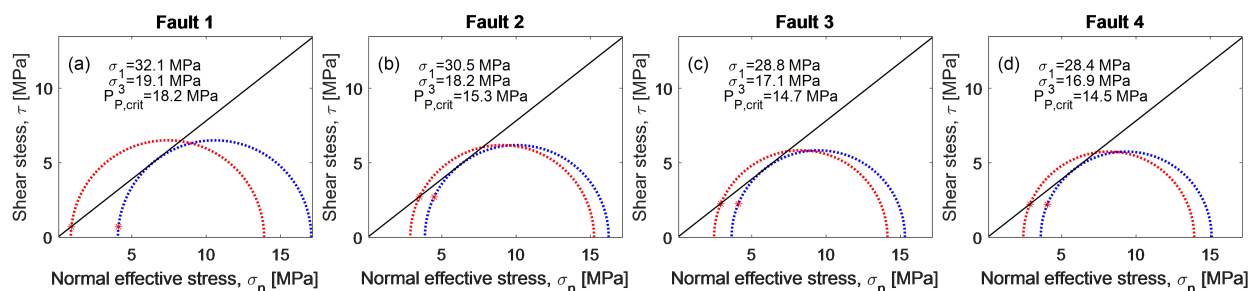


Figure 9. Effective stress Mohr circles at initial pore pressure (blue) and critical pore pressure (red). Red star shows the state of stress at Fault 1 (a), Fault 2 (b), and Fault 3 (c). In-situ stresses are assumed based on stress limit equilibrium. Results illustrate the effect of pore pressure increase at faults.

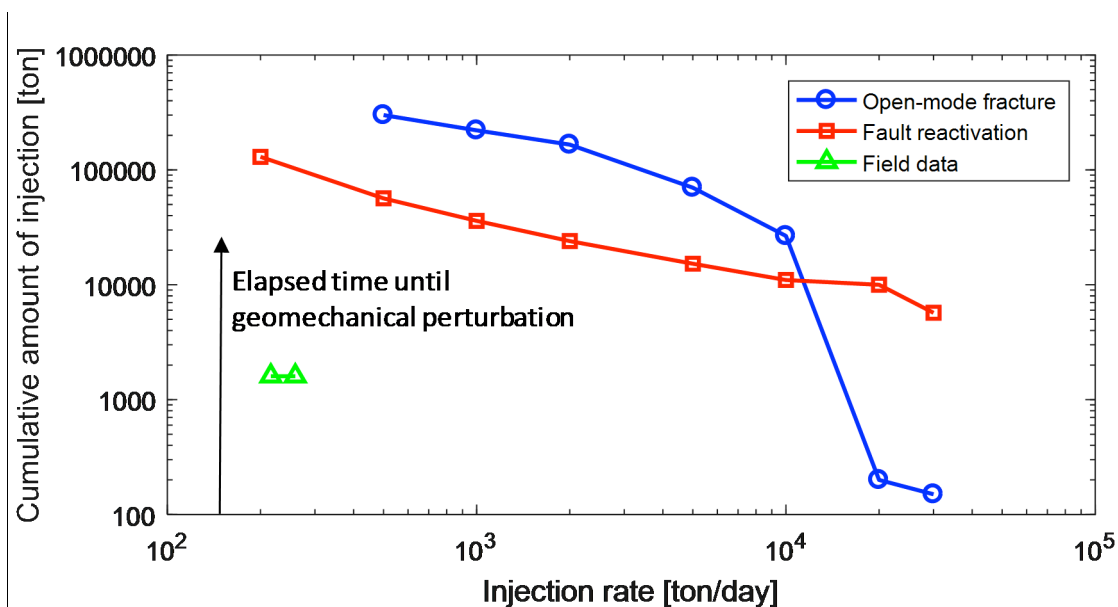


Figure 10. The cumulative amount of CO<sub>2</sub> injection without causing fault reactivation (red line) or hydraulic fracture at the injector (blue line) as a function of injection rate assuming closed reservoir compartments. Green triangles show actual cumulative CO<sub>2</sub> injection volume and injection rates attained in the field during the first Frio pilot test.